RESEARCH

A multi-functional composite nanocatalyst for the synthesis of biologically active pyrazolopyranopyrimidines: Multifaceted antimicrobial, antioxidant, and anticancer activities

Yi Xu[1] · Shefa Mirani Nezhad[2] · Ehsan Nazarzadeh Zare[2] · Seied Ali Pourmousavi[2] · Alireza Doostian[3] · Junna Ren[4] · Ana Cláudia Paiva-Santos[5,6] · Aimin Wu[7] · Gautam Sethi[8] · Filippo Rossi[9] · Xiangdong Wang[10] · Pooyan Makvandi[11]

Abstract

Metal-organic frameworks (MOFs) are crystalline entities made up of metal ions or clusters coordinated to typically rigid organic molecules, creating three-dimensional porous networks. The integration of both inorganic and organic components results in almost unlimited chemical and structural possibilities. This potential has led to MOF for catalytic applications attracting great interest. In this context, a novel multifunctional magnetic nanocomposite, was synthesized for the efficient and sustainable production of biologically active pyrazolopyranopyrimidines. This composite (Fe_3O_4@P*m*PDA@UiO-66-NH_2) combines the advantages of magnetic nanoparticles (Fe_3O_4), a polymer coating poly(*meta*-phenylenediamine), and a metal-organic framework (UiO-66-NH_2). The nanocomposite as a multifunctional magnetic catalyst has been synthesized in three steps including (1) synthesis of Fe_3O_4 nanoparticles by *co*-precipitation technique (2) preparation of UiO-66-NH_2 through a solvothermal method, (3) preparation of nanoparticles-polymer-MOF hybrid nanocomposite using Fe_3O_4, P*m*PDA, and UiO-66-NH_2. The prepared catalyst was fully characterized by XRD, FTIR, EDX, FESEM, TGA, and VSM analyses. The Fe_3O_4@P*m*PDA@UiO-66-NH_2 nanocomposite was used as a catalyst for the synthesis of pyrazolopyranopyrimidines. Various pyrazolopyranopyrimidine products were synthesized in remarkable yields (90–96%) in a short reaction time (10–80 min). The biological activity of pyrazolopyranopyrimidines was studied. The anticancer evaluation of some pyrazolopyranopyrimidines was studied on the survival rate of HepG2 cancer cells and NIH/3T3 fibroblast cells by using an MTT assay. A greater inhibition of cell viability was obtained after 48 h of incubation with higher concentrations (150 µg/L) of pyrazolopyranopyrimidines compounds, demonstrating the anti-proliferative effects of these agents. Additionally, in most cases, the viability of fibroblast cells exhibited a comparatively minor decline when incubated with pyrazolopyranopyrimidines as opposed to HepG2 cells. Furthermore, these compounds have an antioxidant activity between 85.3 and 98.3%. Additionally, their antimicrobial activity was evaluated using the Kirby-Bauer disk diffusion method and showed the highest inhibition zone against *Staphylococcus aureus* and *Escherichia coli* of 19 ± 2.0 and 10 ± 1.5 mm, respectively.

Abbreviations

PmPDA	Poly (meta-phenylenediamine)
MOF	Metal-Organic Framework
MNPs	Magnetic nanoparticles
APTES	3-Aminopropyl triethoxysilane
THAM	Tris (hydroxymethyl) aminomethane
APS	Ammonium persulfate
NPs	Nanoparticles
EtOH	Ethanol
THF	Tetrahydrofuran
DMSO	Dimethyl sulfoxide
DMF	Dimethylformamide
DPPH	2,2-diphenyl-1-picrylhydrazyl
BDC-NH2	2-amino terephthalic acid
r.t.	Room temperature
HepG2	Hepatoblastoma cell line
MTT	3-(4,5-dimethylthiazol-2-yl)-2,5-diphenyltetrazolium bromide
NR	Not reported
NE	No effect
FTIR	Fourier transform infrared spectroscopy
XRD	X-ray diffraction

Yi Xu and Shefa Mirani Nezhad are co-first author.

Extended author information available on the last page of the article

FESEM	Field emission scanning electron microscope
TGA	Thermogravimetric analysis
VSM	Vibrating sample magnetometer
BET	Brunauer-Emmett-Teller
$a_{s,\ BET}$	Specific surface area

1 Introduction

Because of their tunable functionality, specific surface structures, and diverse synthesis methods, metal-organic frameworks (MOFs) are extensively applied in drug delivery [1–4] adsorption [5–7], sensing [8, 9], photocatalyst [10–12], gas capture, storage, and separation [13, 14], carbon dioxide adsorption [15, 16], and catalysis [17, 18]. Several studies have been conducted on the catalytic applications of different derivatives of MOFs. For instance, Palladium nanoparticle-decorated MOF(Zr)@Guanidine catalyst in cross-coupling reactions [19], β-cyclodextrin incorporated UiO-66-NH$_2$ for the C–C coupling reaction [20], UiO-66 catalyzed arylation of enol acetates [21], and bimetallic Cu-Zn(BDC)-MOF catalyzed reduction of organic dyes reaction [22].

An octahedral structure was first described for the material UiO-66 (Zr). Compared to other MOFs, the biggest advantage of UiO-66-NH$_2$ is its combination of excellent thermal, chemical, anti-mechanical, and water stability, along with its exceptional catalytic properties. UiO-66-NH$_2$ demonstrates remarkable catalytic activity due to its high surface area, well-defined porosity, and the presence of amino functional groups, which enhance its reactivity and efficiency in various catalytic processes [23, 24]. UiO-66-NH$_2$ is well-known for its high surface area and porous structure, which are vital for enhancing catalytic activity and providing ample active sites for reactions. Its large pore size facilitates the diffusion of reactants and products, making it an excellent candidate for catalytic applications. The amino groups present in UiO-66-NH$_2$ significantly enhance its reactivity and interaction with substrates. These functional groups play a pivotal role in the catalytic process, allowing for efficient synthesis of biologically active compounds. The functionalization also contributes to the stability and tunability of the MOF, which is advantageous for various chemical transformations. UiO-66-NH$_2$ has been demonstrated to exhibit good biocompatibility, which is essential for applications involving biological systems. Its stability in aqueous environments and low cytotoxicity make it suitable for pharmaceutical and biomedical applications [25–27].

UiO-66-NH$_2$ frameworks are widely utilized for the conjugation of pharmaceuticals. Their significant surface area, diverse pore dimensions, and straightforward functionalization have led to extensive research into the biomedical potential of UiO-66 metal-organic frameworks (MOFs). The biocompatibility of these MOFs has been examined through numerous in vitro and in vivo studies. Fe$_3$O$_4$ nanoparticles have emerged as promising materials in biomedicine due to their favorable properties, including good biocompatibility, low toxicity, and strong magnetic responsiveness. These nanoparticles hold potential for various applications like disease diagnosis and cancer treatment. To enhance their biocompatibility and targeting abilities, magnetic nanoparticles (MNPs) are typically coated with materials such as inorganic substances, organic molecules, or polymers, creating a protective shell that prevents clumping and allows for targeted delivery. The magnetic properties of MNPs enable their use for in vivo applications, including improved medical imaging resolution and targeted heating for therapeutic purposes at the site of injury or disease. Previous investigations into UiO-66 MOFs have indicated that UiO-66 with low cytotoxicity holds considerable promise for applications in biomedicine, particularly in drug delivery systems magnetic metal-organic framework composites (MMOF) consist of two primary elements: MNPs and MOF structures. The high stability of MMOF composites renders them ideal for utilization as drug carriers in applications involving cells [28–30].

Homogeneous catalysts offer high activity and selectivity due to their dissolved nature in the reaction medium. Due to the difficult separation, however, their recycling is complex and expensive. On the other side, classical heterogeneous catalysts in industry often have lower activity and selectivity because of steric and diffusion factors. To improve catalyst activity and selectivity, nanoscale metal-based catalysts and supports have been proposed. Nanometer-sized supports increase surface area and form homogenous emulsions. Magnetic nanoparticles are particularly favored as catalyst supports because of their high surface area, stability, high loading capacity, and ease of recycling. Magnetic separation simplifies catalyst recovery and tolerates most chemical environments except highly acidic or corrosive environments. Magnetic nanocomposites of various materials and compositions are used in a wide range of applications from engineering to biomedical fields [31, 32]. Pyrazolopyranopyrimidines are polycyclic heterocycles composed of pyrazole, pyrimidine, and pyran units. The pyranopyrazole segment is important in the pharmaceutical industry and is responsible for a variety of biological properties of molecules containing this segment. Such compounds may act as anticancer agents [33], analgesic, and anti-inflammatory [34], antimicrobial [35], antiplatelet [36], and antioxidant activity [37]. The pyranopyrimidine moiety, found in natural products is known for its biological activities such as anti-diabetic [38], antimicrobial [39], anticancer agents [40], and antifungal activity [41].

Numerous protocols developing derivatives of pyrazolopyranopyrimidines have been reported in recent years. For example, the use of sulfonic acid functionalized

1,4-diazabicyclo[2.2.2]octane supported on Merrifield resin [42], using triazole-bonded silica heterogeneous [43], Fe_3O_4@tris(hydroxymethyl) aminomethane (THAM)-piperazine [44], choline chloride: urea deep eutectic solvent [45], ultrasoundassisted [46], tetramethyl guanidin functionalized nanosize γAl_2O_3 [47], $CoFe_2O_4$@SiO_2-3-aminopropyl)triethoxysilane (APTES)-cyanuric chloride-guanidine [48], 1,8-diazabicyclo(5.4.0)undec-7-ene based Fe_3O_4@$nSiO_2$@$mSiO_2$ nanomagnetic [49], and $ZnFe_2O_4$/glutamic acid [50].

This study focuses on the development of a novel multifunctional magnetic nanocomposite (Fe_3O_4@P*m*PDA@UiO-66-NH_2). We will evaluate the catalytic performance of Fe_3O_4@P*m*PDA@UiO-66-NH_2 in the synthesis of pyrazolopyranopyrimidines, focusing on key parameters such as reaction yield and reaction time. Furthermore, the reusability and stability of the catalyst under different reaction conditions will be investigated to assess its potential for sustainable and cost-effective synthesis. The biological activity of pyrazolopyranopyrimidines will be examined, with their anticancer effects on the survival rates of HepG2 cancer cells and NIH/3T3 fibroblast cells evaluated using the MTT assay. Additionally, the study will assess their antioxidant properties using the DPPH radical scavenging test and investigate their antimicrobial activity against *Staphylococcus aureus* and *Escherichia coli.*

2 Experimental

2.1 Synthesis of UiO-66-NH_2

To synthesize UiO-66-NH_2, a mixture of 125 mg of $ZrCl_4$, 1 mL of concentrated HCl, and 5 mL of DMF was placed in a 100 mL vial and sonicated for 20 min to ensure complete dissolution. Then, 134 mg of BDC-NH_2 (2-amino terephthalic acid) dissolved in 10 mL of DMF was added to the vial. The reaction mixture was sonicated for an additional 20 min and then heated at 80 °C overnight. Following the reaction, the nanoparticles were collected by centrifugation, the supernatant was removed, and the nanoparticles were resuspended in DMF and centrifuged twice to wash them. Finally, the nanoparticles were suspended in ethanol and centrifuged again (Fig. 1A).

2.2 Synthesis of Fe_3O_4 nanoparticles

For the synthesis of Fe_3O_4 nanoparticles, $FeCl_2 \cdot 4H_2O$ (2.1 mmol) and $FeCl_3 \cdot 6H_2O$ (4.9 mmol) were dissolved in deionized water. The mixture was mechanically stirred at 80 °C for 15 min, and then a 10% NaOH solution was added until the pH reached 10. After 30 min, the black precipitate was separated magnetically and washed several times with deionized water and twice with ethanol (Fig. 1B).

2.3 Synthesis of Fe_3O_4@PmPDA@UiO-66-NH_2

In a 250 mL flask, 0.3 g of Fe_3O_4 nanoparticles and 0.35 g of UiO-66-NH_2 were sonicated in 20 mL of distilled water for 30 min. Next, 1 g of *meta*-phenylenediamine monomer was dissolved in 100 mL of 0.1 M HCl solution and added to the reaction mixture. The mixture was sonicated for another 30 min until the monomer was completely dissolved. Polymerization was initiated by adding 10 mL of ammonium persulfate (APS) in 0.1 M HCl solution over 1 h under magnetic stirring at room temperature. The reaction mixture was continuously stirred in a nitrogen atmosphere for 24 h. The resulting nanocomposite was separated using an external magnet, washed several times with water and methanol, and dried in a vacuum oven at 50 °C for 12 h (Fig. 1C).

2.4 General procedure for the synthesis of 3-substituted 1-phenyl-1 H-pyrazol-5-ol

The synthesis of 3-substituted-1-phenyl-5-pyrazolone was carried out by reacting ethyl acetoacetate or ethyl benzoylacetate with phenylhydrazine in a 1:1 molar ratio in ethanol. Acetic acid was added as a catalyst, and the mixture was stirred for 2 h under reflux conditions. After cooling, the crude solid product was filtered and purified by recrystallization from ethanol (Fig. 2A).

2.5 General route for the preparation of pyrazolopyranopyrimidines

To prepare pyrazolopyranopyrimidines, a mixture of 3-substituted-1-phenyl-1*H*-pyrazol-5-ol (1.0 mmol), an aldehyde (1.0 mmol), barbituric acid (1.0 mmol), and Fe_3O_4@P*m*PDA@UiO-66-NH_2 (0.05 g) in 5 mL of ethanol was stirred at room temperature. The progress of the reaction was monitored using thin-layer chromatography (ethyl acetate/hexane 5:1) until completion. The catalyst was then separated using an external magnet. The resulting crude solid product was filtered and purified by crystallization in ethanol (Fig. 2B).

2.6 In vitro cell viability assay

To evaluate the cytotoxicity of the synthesized compounds, an MTT assay was performed following previously described methods [33]. Briefly, HepG2 cancer cells and NIH/3T3 fibroblast cells were seeded at a density of 5×10^3 cells per well in 96-well plates and incubated overnight at 37 °C in a humidified 5% CO_2 atmosphere. The next day,

Fig. 1 The synthesis procedure of UiO-66-NH$_2$(**A**), Fe$_3$O$_4$ (**B**), and Fe$_3$O$_4$@P*m*PDA@UiO-66-NH$_2$ (**C**)
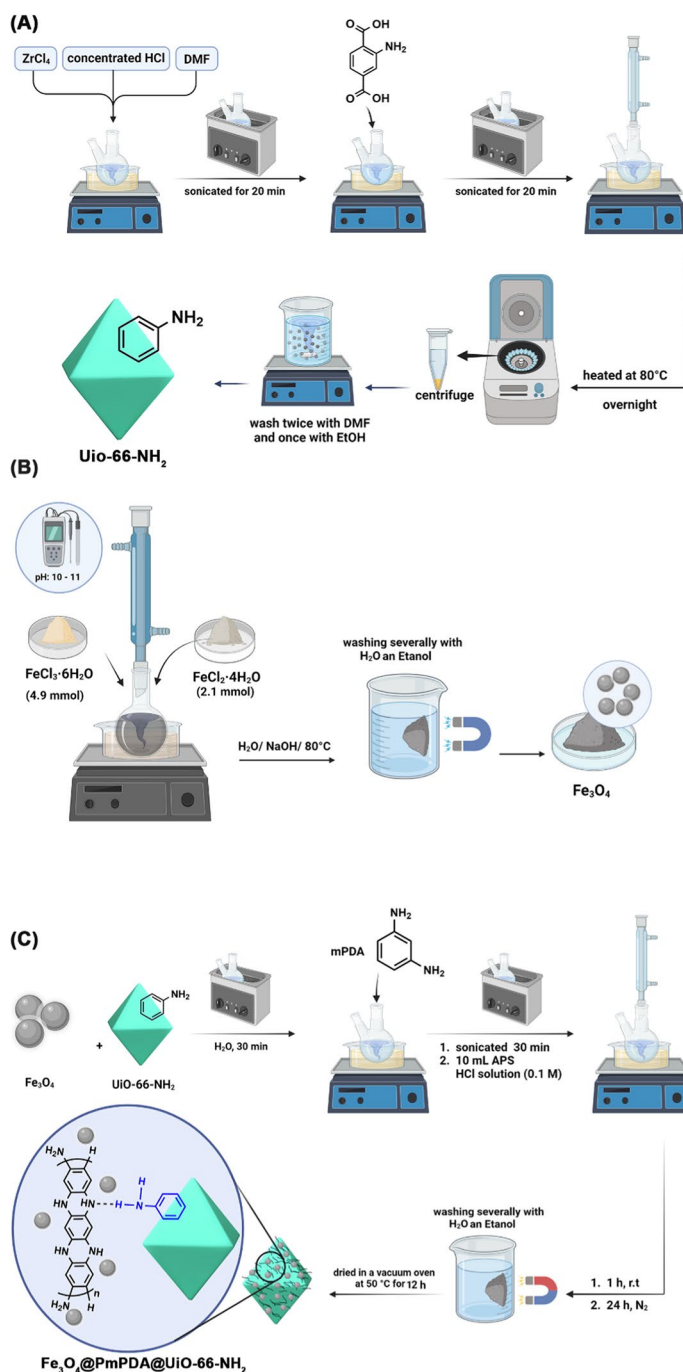

the cells were treated with various concentrations of the synthesized compounds (150, 75, 37.5, 18.75, 9.375, and 0 µg/mL) for 24 and 48 h. After the incubation periods, MTT solution (5 mg/mL) was added to each well, and the plates were incubated further at 37 °C for 4 h. The medium was then removed, and 200 µL of DMSO was added to each well to dissolve the formazan crystals. The absorbance of the solubilized purple formazan was measured at 540 nm using a microplate spectrophotometer (BioTek, USA). The cell viability percentage was calculated as follows:

$$[(Absorbance\ of\ untreated\ cells - Absorbance\ of\ treated\ cells)\ /Absorbance\ of\ untreated\ cells] * 100$$

Fig. 2 Preparation of 3-substituted-1-phenyl-1*H*-pyrazol-5-ol (**A**) and pyrazolopyranopyrimidines (**B**)
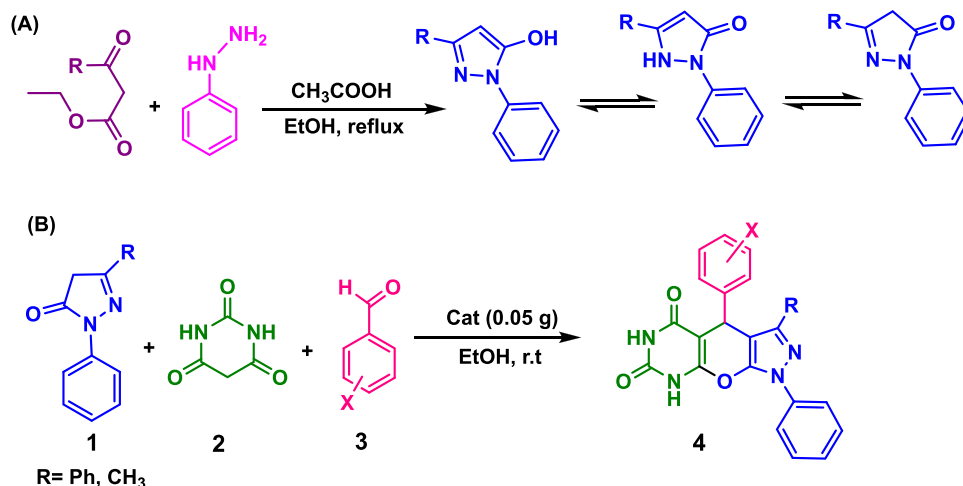
2.7 In vitro antioxidant activity measurement

To assess antioxidant activity of pyrazolopyranopyrimidines, we used a common method DPPH radical scavenging assay. In this test, 120 mg of pyrazolopyranopyrimidine samples were added to 3.20 mL of ethanolic DPPH solution (100 mM). The mixture was incubated in the dark for 30 min. As a result, this process leads to a shift of the DPPH free radical from purple to DPPH-H yellow, which is related to the number of electrons captured. After incubation, the mixture was centrifuged and the absorbance of the remaining DPPH concentration of the supernatant was measured with a UV-Vis spectrometer at a wavelength of 517 nm. A reduction in the absorbance of the DPPH solution signifies an enhancement in antioxidant activity. The calculation of DPPH inhibition was performed using the following specified formula [51, 52].

$$\% \text{ of DPPH inhibition} = \frac{A_b - A_s}{A_b} \times 100$$

where A_b is the absorption of the ethanolic DPPH solution and A_s is the absorption of the sample in ethanolic DPPH solution.

2.8 In vitro antibacterial activity measurement

The antimicrobial activity of the samples was assessed using the Kirby-Bauer disk diffusion method, a standard technique for determining the susceptibility of bacteria to antibiotics [53]. The bacterial cultures were evenly distributed on Mueller-Hinton agar plates. Sterile paper disks were loaded with a concentration of 50 μL of each sample suspension (20 mg/mL) and placed on top of the inoculated agar. The plates were then incubated at 4 °C for one hour to allow the sample to diffuse into the agar medium. After incubation, plates were placed in an incubator at 37 °C for 24 h to allow bacterial growth. The size of the inhibition zone was measured in millimeters to determine the antimicrobial activity of the sample [54]. The results were presented as mean and standard deviation ($\pm$ SD). aztreonam (30 μg/disc), tetracycline

Fig. 3 FTIR spectra (**A**) and TGA curves (**B**) of P*m*PDA, UiO-66-NH$_2$, and Fe$_3$O$_4$@P*m*PDA@UiO-66-NH$_2$
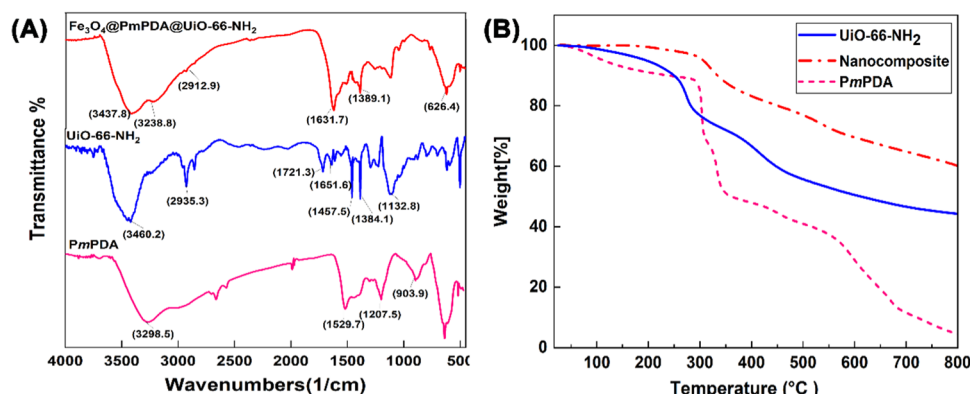
(30 µg/disc), imipenem (10 µg/disc), nitrofurantoin (300 µg/disc), and rifampin (5 µg/disc) were applied as a positive control.

3 Results and discussions

3.1 Characterization of nanocatalyst

Figure 3A shows FT-IR spectra of PmPDA, UiO-66-NH$_2$, and Fe$_3$O$_4$@PmPDA@UiO-66-NH$_2$. The peaks in the spectrum of UiO-66-NH$_2$ related to the symmetric and asymmetric stretching of the carboxyl functional groups UiO-66-NH$_2$ appeared at 1300–1700 cm^{-1}. The peak at 1457 cm^{-1} is related to the result of the stretching of the aromatic C—C bonds, and the broad absorption peak at 3460 cm^{-1} is related to the —NH$_2$ groups in the 2-aminoterephthalic acid structure of UiO-66-NH$_2$. In the FT-IR spectrum of PmPDA, the two characteristic peaks at 1529 and 1510 cm^{-1} correspond to the stretching of the amine quinoid and amine benzenoid units. the peaks around 3200 and 3490 cm^{-1} correspond to the stretching vibration of the —NH$_2$ and N—H groups. After modifying UiO-66-NH$_2$ with Fe$_3$O$_4$ and PmPDA, the FTIR spectrum of the composite shows that the intensity of the peaks assigned to PmPDA becomes more prominent and the peaks corresponding to UiO-66-NH$_2$ are greatly reduced.

TGA was used to evaluate the thermal stability of PmPDA, UiO-66-NH$_2$, and Fe$_3$O$_4$@PmPDA@UiO-66-NH$_2$.

The UiO-66-NH$_2$ thermogram in Fig. 3B shows weight loss in three main stages. The first weight loss associated with loss of surface moisture and solvent occurs at about 100 °C. The second weight loss, which occurs at around 200–250 °C, is associated to the loss of DMF (solvent) from the pores of the MOFs as well as the loss of coordinated water molecules within the cage in the MOF structure. The third weight loss at about 400–500 °C is due to the destruction of organic bonds and structural degradation of MOFs [55, 56]. The degradation of PmPDA occurs in three steps. The first weight loss at around 100 °C is related to the removal of moisture, HCl, and solvent trapped in the polymer backbone. The second weight loss is related to the removal of low molecular weight oligomers and the third weight loss (40%), which occurs at about 400 to 600 °C, is due to the destruction of the main chains of the polymer. When comparing the thermograms of UiO-66-NH$_2$, PmPDA, and Fe$_3$O$_4$@PmPDA@UiO-66-NH$_2$, it was observed that Fe$_3$O$_4$@PmPDA@UiO-66-NH$_2$ exhibited higher stability than the other samples. This enhanced stability is likely due to the strong bonding interactions between the hydroxyl groups of Fe$_3$O$_4$ nanoparticles and the amine groups on PmPDA and UiO-66-NH$_2$ [57]. TGA analysis indicates that the catalyst exhibits minimal weight loss up to 300 °C, demonstrating considerable thermal stability, which suggests its suitability for high-temperature reactions.

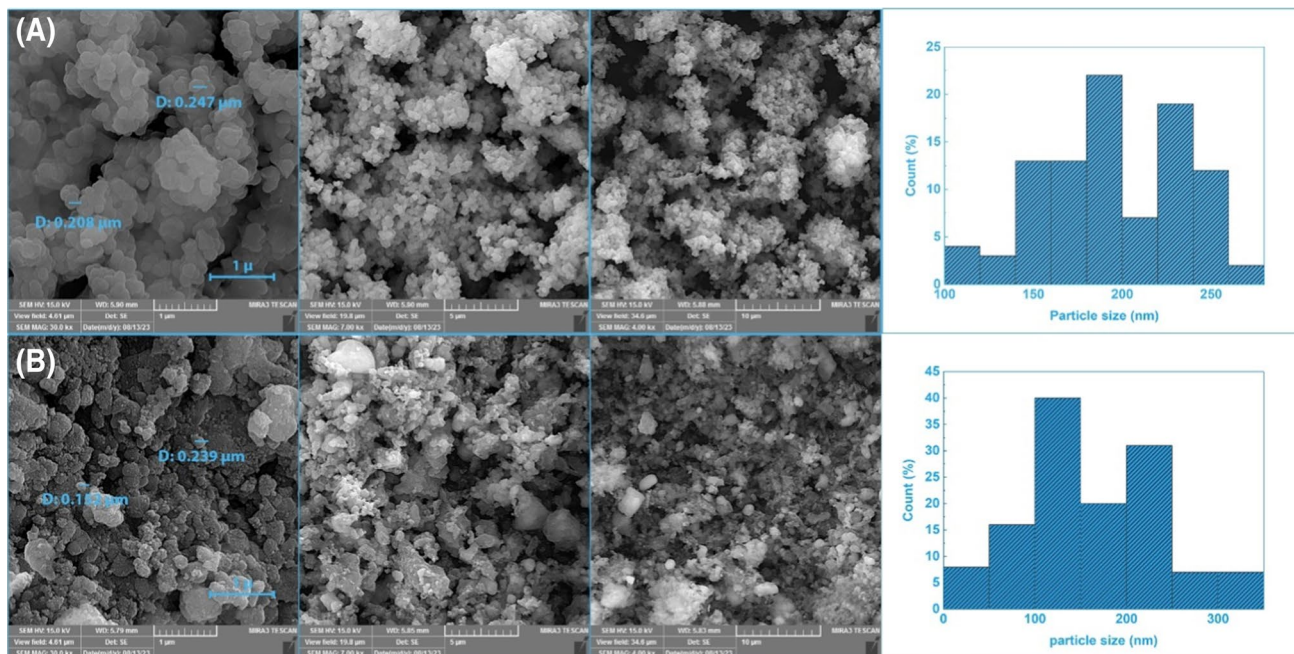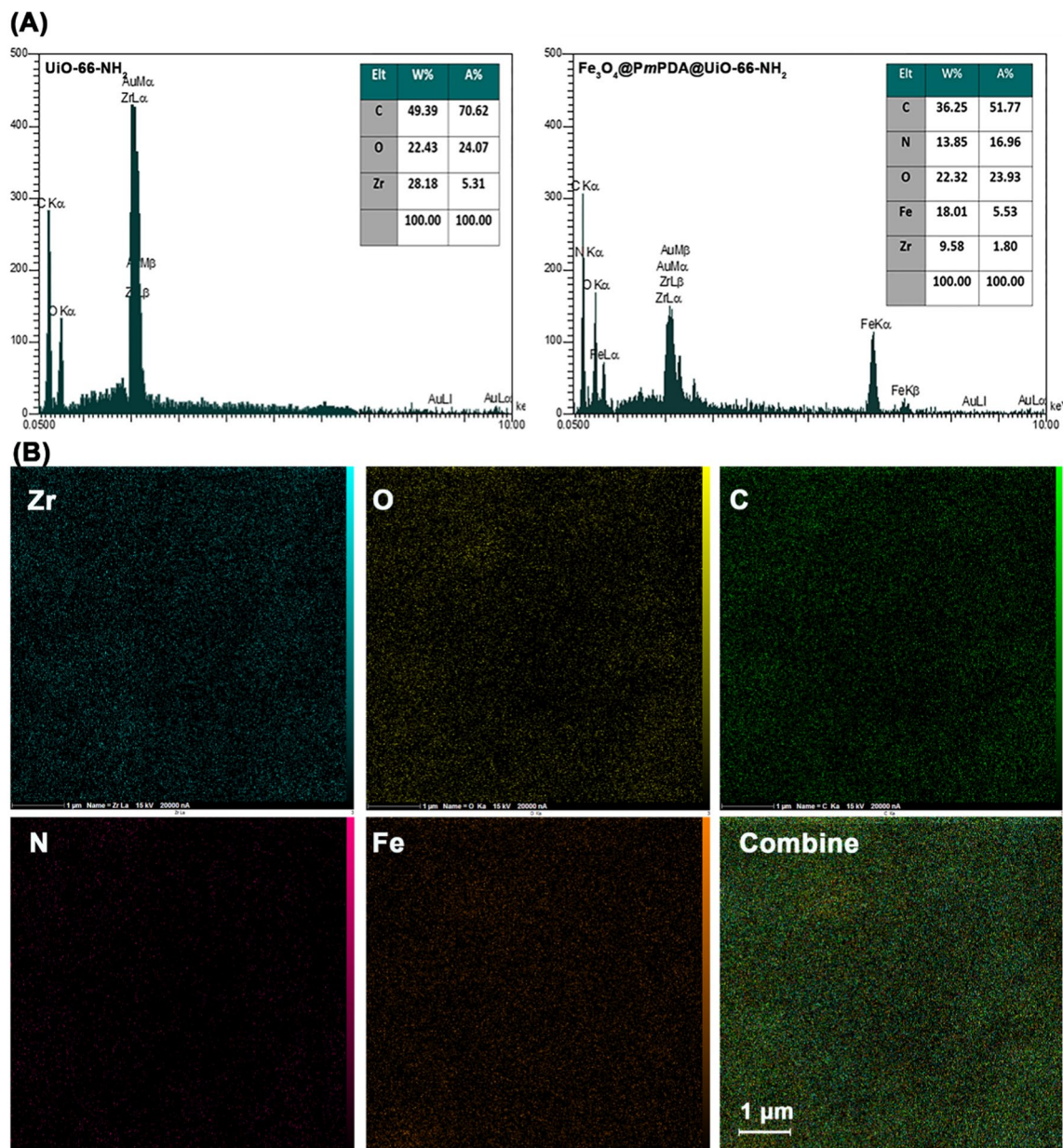Based on the results of FESEM, UiO-66-NH$_2$ was synthesized with the morphology of semi-cubic. FESEM images

**Fig. 4** FESEM micrographs of UiO-66-NH2 (**A**), and Fe3O4@PmPDA@UiO-66-NH2 (**B**)

Fig. 5 EDX spectra and tabulated data of UiO-66-NH$_2$ and Fe$_3$O$_4$@P*m*PDA@UiO-66-NH$_2$ **(A)** and EDX mapping of Fe$_3$O$_4$@P*m*PDA@UiO-66-NH$_2$ **(B)**

in Fig. 4A showed regularly shaped particles in the range of 150 to 250 nm. After adding Fe$_3$O$_4$ and P*m*PDA to UiO-66-NH$_2$, morphology was changed; aggregations were observed due to adding an organic structure and nanoparticles (Fig. 4B). Increasing the specific surface area by reducing the particle size of the catalyst particles can significantly influence the activity of a reaction. Smaller particles have a higher surface area to volume ratio, resulting in more active sites for chemical reactions.

The chemical composition of UiO-66-NH$_2$ and Fe$_3$O$_4$@P*m*PDA@UiO-66-NH$_2$ was analyzed by the EDX (Fig. 5A).

The presence of Zr, O, and C in the UiO-66-NH$_2$, and O, Zr, C, Fe, and N in the Fe$_3$O$_4$@P*m*PDA@UiO-66-NH$_2$ confirmed the formation of MOF and nanocomposite. Furthermore, Fig. 5B shows the EDX mapping of Fe$_3$O$_4$@P*m*PDA@UiO-66-NH$_2$ which approved the presence of Zr, C, O, Fe, and N in the nanocomposite. The EDX mapping shows the uniform distribution of all elements and the active site on the catalyst.

The magnetic properties of Fe$_3$O$_4$ nanoparticles and the Fe$_3$O$_4$@P*m*PDA@UiO-66-NH$_2$ nanocomposite were studied using a technique called vibrating sample
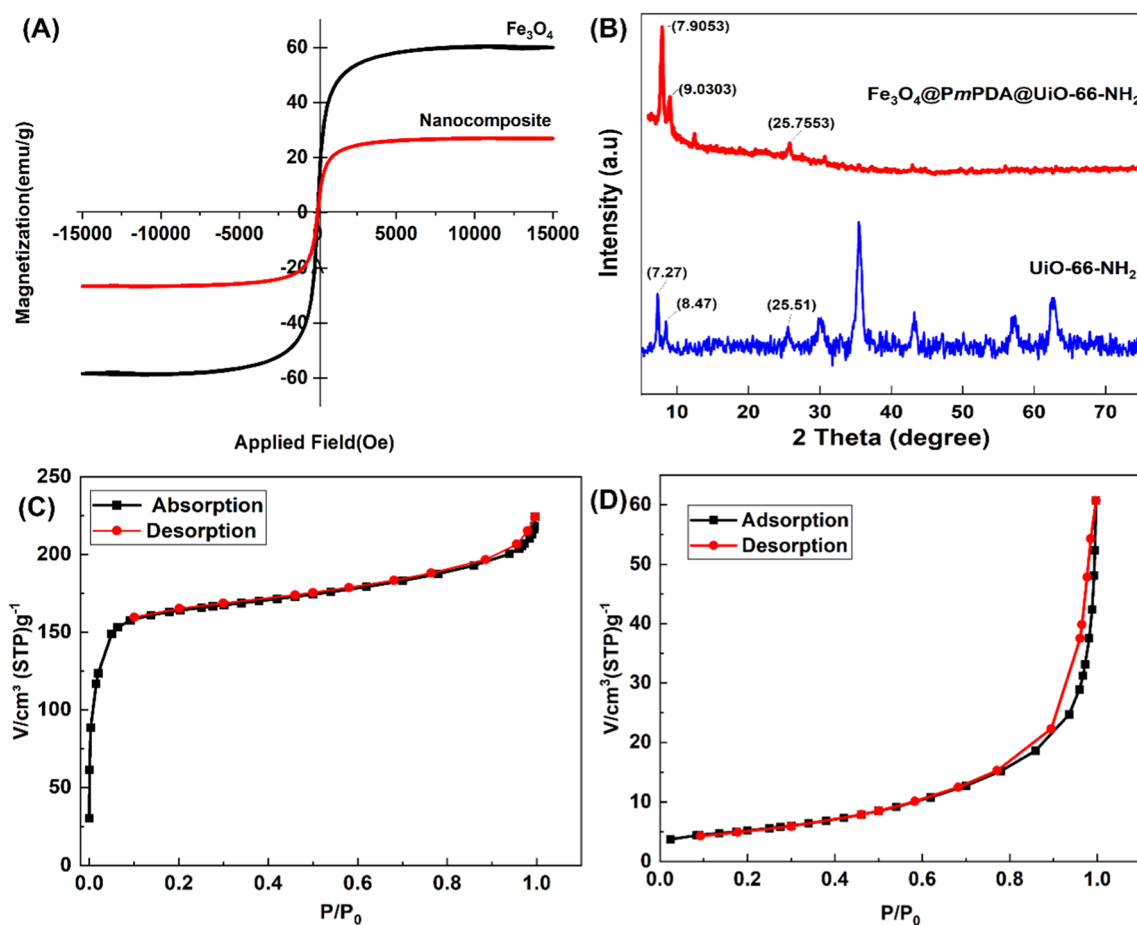
Fig. 6 VSM curves of Fe_3O_4 nanoparticles and Fe_3O_4@P*m*PDA@UiO-66-NH$_2$nanocomposite **(A)**, XRD patterns ofUiO-66-NH$_2$and Fe_3O_4@P*m*PDA@UiO-66-NH$_2$ **(B)**, N$_2$ adsorption/desorption isotherm UiO-66-NH$_2$ **(C)** and Fe_3O_4@P*m*PDA@UiO-66-NH$_2$ nanocomposite **(D)**

magnetometry (VSM) (Fig. 6A). The results showed that the Fe_3O_4 nanoparticles had a saturation magnetization of 60.29 emu/g, which means they have strong magnetic properties. In contrast, the Fe_3O_4@P*m*PDA@UiO-66-NH$_2$ nanocomposite had a lower saturation magnetization of 27.94 emu/g. This decrease is due to the non-magnetic coatings (P*m*PDA and UiO-66-NH$_2$) added to the Fe_3O_4 particles. Even though the magnetization is lower in the nanocomposite, it still has good magnetic properties that allow for easy separation of the catalyst from the reaction solution. This makes it easier to recycle the catalyst, reducing costs and promoting more sustainable and eco-friendly methods for producing chemical reactions [58].

Based on the XRD pattern, the characteristic diffraction peaks of UiO-66-NH$_2$ appeared at $2\theta = 7.2$, 8.4, and 25.5 in the XRD pattern, indicating the successful synthesis of NH$_2$-UiO-66 (Fig. 6B) [59]. XRD patterns of Fe_3O_4@P*m*PDA@UiO-66-NH$_2$ nanocomposite showed a semi-crystalline nature. The peaks appearing in 7.9, 9.0, and 25.7 corresponds to UiO-66-NH$_2$.

As shown in Fig. 6C-D, Brunauer-Emmett-Teller (BET) analysis was applied to define the specific surface area of the material and evaluate the effect of the existing surface coating of UIO-66-NH$_2$ with Fe_3O_4 nanoparticles and P*m*PDA. The specific surface area ($a_{s, BET}$) values of UiO-66-NH$_2$ and Fe_3O_4@P*m*PDA@UiO-66-NH$_2$ nanocomposite were 545.9569 ± 11.8746 m^2/g and 18.5229 ± 0.0215 m²/g, respectively. The isotherms of Fe_3O_4@P*m*PDA@UiO-66-NH$_2$ displayed a discrepancy between the desorption and adsorption curves at relative pressures below 0.4. This observation indicates the presence of micropores that promote increased capillary condensation at the reduced pressures required for evaporation and desorption [35]. The reduction in surface area of Fe_3O_4@P*m*PDA@UiO-66-NH$_2$ compared to UiO-66-NH$_2$ could be due to the encapsulation of Fe_3O_4 nanoparticles and P*m*PDA in the porous structure of UiO-66 [60]. The obtained results confirmed the FESEM images of Fe_3O_4@P*m*PDA@UiO-66-NH$_2$. When the nanoparticles in the structure of the catalyst are placed on the surface of the high porosity substrate, they increase the reaction efficiency and reduce the

Table 1 Optimization of the 3-methyl-1-phenyl-1*H*-pyrazol-5-ol, benzaldehyde, and barbituric acid reaction[a]

Entry	Solvent	Catalyst (g)	Temp /$^\circ$C	Time (Min)	Yield %[b]
1	Solvent-free	Fe_3O_4@P*m*PDA@UiO-66-NH$_2$ (0.03)	r.t	360	30
2	H_2O	Fe_3O_4@P*m*PDA@UiO-66-NH$_2$ (0.03)	r.t	360	45
3	Methanol	Fe_3O_4@P*m*PDA@UiO-66-NH$_2$ (0.03)	r.t	75	90
4	EtOH	Fe_3O_4@P*m*PDA@UiO-66-NH$_2$ (0.03)	r.t	80	90
5	H_2O/EtOH	Fe_3O_4@P*m*PDA@UiO-66-NH$_2$ (0.03)	r.t	360	50
6	CH_3CN	Fe_3O_4@P*m*PDA@UiO-66-NH$_2$ (0.03)	r.t	360	80
7	THF	Fe_3O_4@P*m*PDA@UiO-66-NH$_2$ (0.03)	r.t	360	65
8	CH_2Cl_2	Fe_3O_4@P*m*PDA@UiO-66-NH$_2$ (0.03)	r.t	360	60
9	Hexane	Fe_3O_4@P*m*PDA@UiO-66-NH$_2$ (0.03)	r.t	360	20
10	Ethyl acetate	Fe_3O_4@P*m*PDA@UiO-66-NH$_2$ (0.03)	r.t	360	65
11	DMF	Fe_3O_4@P*m*PDA@UiO-66-NH$_2$ (0.03)	r.t	120	85
12	EtOH	Fe_3O_4@P*m*PDA@UiO-66-NH$_2$ (0.03)	40	80	85
13	EtOH	Fe_3O_4@P*m*PDA@UiO-66-NH$_2$ (0.03)	60	80	70
14	EtOH	Fe_3O_4@P*m*PDA@UiO-66-NH$_2$ (0.03)	Reflux	80	Trace
15	EtOH	-	r.t	360	Trace
16	EtOH	Fe_3O_4@P*m*PDA@UiO-66-NH$_2$ (0.05)	r.t	60	90
17	EtOH	Fe_3O_4@P*m*PDA@UiO-66-NH$_2$ (0.06)	r.t	60	91
18	EtOH	Fe_3O_4 (0.05)	r.t	60	55
19	EtOH	P*m*PDA(0.05)	r.t	60	82
20	EtOH	UiO-66-NH$_2$(0.05)	r.t	60	80

[a]Reaction conditions 3-methyl-1-phenyl-1H-pyrazol-5-ol (1.0 mmol), benzaldehyde (1.0 mmol), barbituric acid (1.0 mmol), [b]isolated yield. *r.t* room temperature

consumption of the catalyst, so the performance of the catalyst depends on the specific surface area of the support [61].

3.2 Catalytic potential study of the Fe_3O_4@P*m*PDA@UiO-66-NH$_2$

The synthesis of pyrazolopyranopyrimidines was investigated using the catalyst Fe_3O_4@P*m*PDA@UiO-66-NH$_2$. The one-pot reaction between benzaldehyde, barbituric acid, and 3-methyl-1-phenyl-1*H*-pyrazol-5-ol was studied to optimize the reaction conditions in the presence of nanocomposite (Table 1). First, the reaction was examined at room temperature and in various solvents and without solvent (**Entries 1–11**). The highest yields and shortest reaction times were obtained in the solvents, ethanol, and methanol. Considering the growing significance of environmentally friendly reaction media in organic synthesis, ethanol was selected as the optimal solvent. We then explored the effect of temperature on the reaction's progress. The results showed that with increasing temperature, the efficient performance of the reaction decreases (**Entries 12–14**). Additionally, the effect of the catalyst amount was investigated, revealing that the reaction requires a catalyst, as no product was formed even after 6 h without it (**Entry 15**). The catalytic activities of Fe_3O_4, P*m*PDA, and UiO-66-NH$_2$ were also examined using the typical reaction. The findings demonstrated
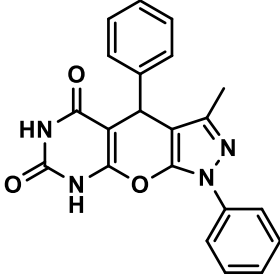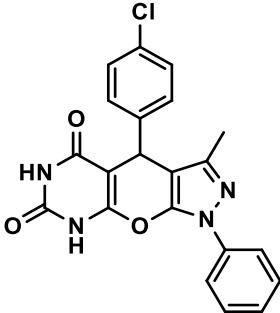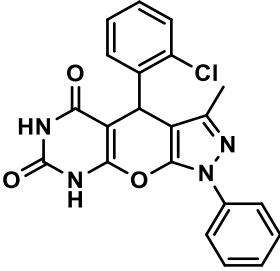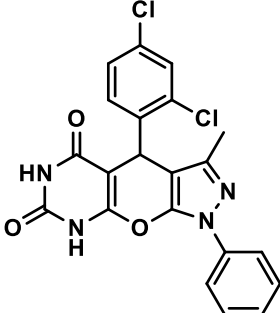
that, compared to other samples, the presence of the catalyst resulted in the products being obtained in a shorter time and with the highest efficiency (**Entries 18–20**).

Different types of aromatic aldehydes were investigated for the synthesis of pyrazolopyranopyrimidines using the optimal amount of (0.05 g Fe_3O_4@P*m*PDA@UiO-66-NH$_2$ (Table 2). The resulting products were purified through crystallization in ethanol and characterized using spectroscopic techniques, specifically ^{1}H-NMR and ^{13}C-NMR.

3.2.1 Proposed mechanism

The suggested reaction mechanism for the synthesis of pyrazolopyranopyrimidines in the existence of Fe_3O_4@P*m*PDA@UiO-66-NH$_2$ is shown in Fig. 7. In this mechanism, first, by activating barbituric acid in the presence of the nanocatalyst, Knoevenagel condensation between benzaldehyde and barbituric acid is performed and intermediate (III) is formed. Then 3-subtituted-1-phenyl-1*H*-pyrazol-5-ol deprotonation is performed by the catalyst. The reaction was followed by Michael's addition of 3-subtituted-1-phenyl-1*H*-pyrazole-5-ol to form intermediate (II) and then intermediate (III). Then intermediate (III) was converted to intermediate (IV) by tautomerization. Subsequently, intramolecular cyclization produces the product by removing H_2O from the intermediate (V).

Table 2 Synthesis of pyrazolopyranopyrimidines by Fe_3O_4@PmPDA@UiO-66-NH_2 and aldehydes[a]

Entry	Product	Code	Time (min.)	Yield[b] (%)	M.P. (°C) Observed	M.P. (°C) Reported	Ref.
1		**4a**	60	90%	208-210	210-211	[62]
2		**4b**	45	94%	200-202	201-204	[63]
3		**4c**	55	90%	172-174		NR
4		**4d**	30	96%	232-2235	234-235	[64]

3.3 Heterogeneity studies

To evaluate the stability of the Fe_3O_4@PmPDA@UiO-66-NH_2 nanocomposite, the hot filtration method was employed. The reaction was carried out under optimized conditions, and after 30 min (just over half the reaction time), the nanocomposite was separated from the hot mixture using a magnet. The reaction mixture was then allowed to proceed for an additional 6 h under the same conditions. The product yield remained constant at 50% after the removal of the nanocomposite catalyst, indicating that the reaction ceases upon isolation of the Fe_3O_4@PmPDA@UiO-66-NH_2 catalyst [65, 66].

Table 2 (continued)

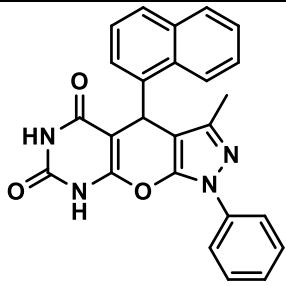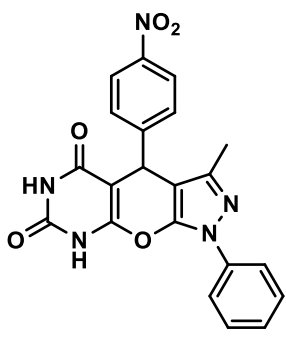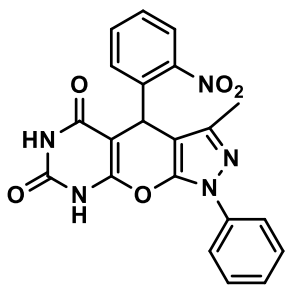|							
5		4e	70	90%	218–220		NR
6		4f	40	95%	222–225	230–232	[64]
7		4g	60	92%	181–183		NR
8		4h	25	94%	180–182		NR
9		4i	30	96%	207–209	207–209	[63]
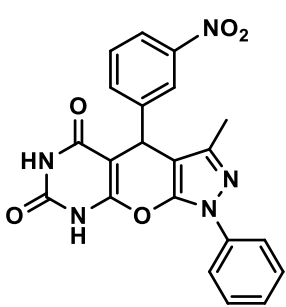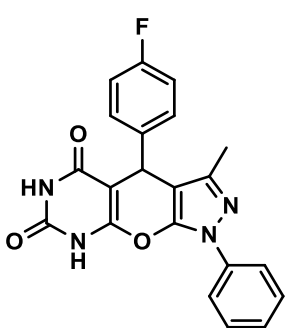
Table 2 (continued)
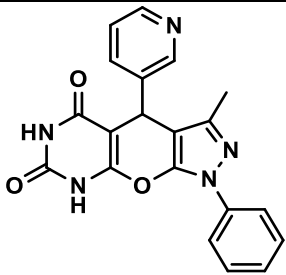
10		**4j**	10	98%	274-276		NR
11		**4k**	15	90%	178-180	170-171	[62]
12		**4l**	60	90%	180-182	NR	NR
13		**4m**	80	92%	207-210	207-209	[62]
14		**4n**	35	95%	184-186	158-159	[63]
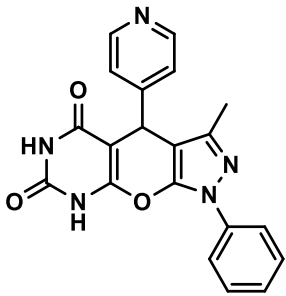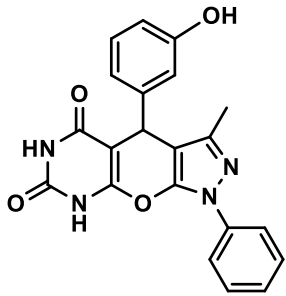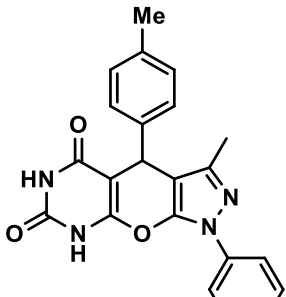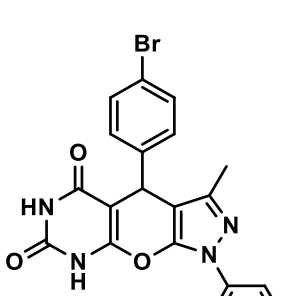
Table 2 (continued)
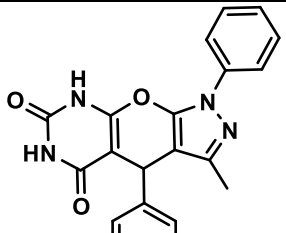
15		**4o**	80	90%	310-312	NR
16		**4p**	60	90%	200-202	NR
17		**4q**	15	94%	283-285	NR
18		**4r**	35	92%	164-166	NR
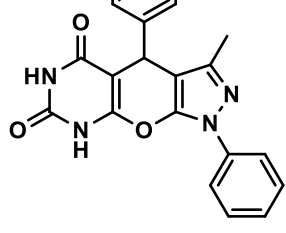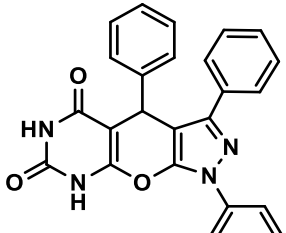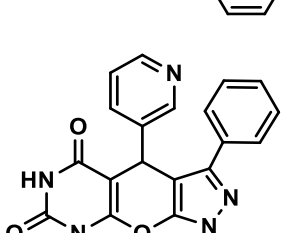
Assessing the catalytic recyclability and reusability is crucial for advancing greener and more sustainable synthetic chemistry practices. The Fe_3O_4@PmPDA@ UiO-66-NH_2 catalyst's ability to be recovered and reused was tested in the reaction involving 3-methyl-1-phenyl-1H-pyrazol-5-ol, benzaldehyde, and barbituric acid to produce compound 4a. After the reaction was completed, the mixture was diluted with ethanol to isolate the nano-catalyst, which was then washed with ethanol and reused for subsequent reactions. The catalyst maintained its performance with minimal loss of activity over five consecutive cycles (Fig. 8).

Table 2 (continued)

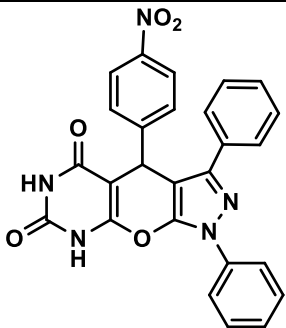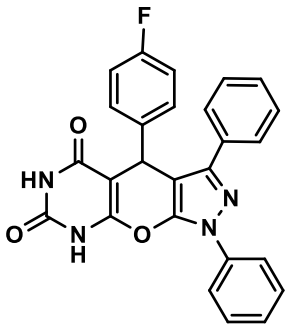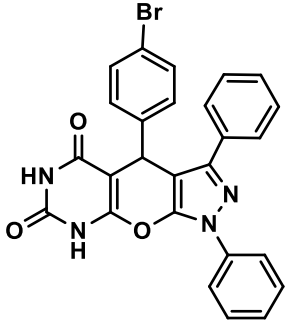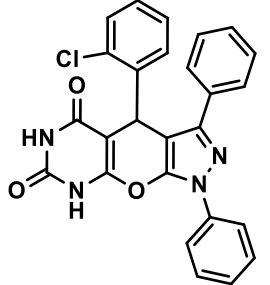|						
19		**4s**	35	95%	206-208	NR
20		**4t**	30	94%	198-200	NR
21		**4u**	25	95%	208-211	NR
22		**4v**	50	90%	219-221	NR
23		**4w**	80	90%	153-155	NR
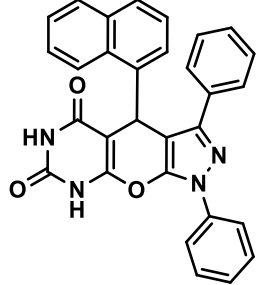
Table 2 (continued)
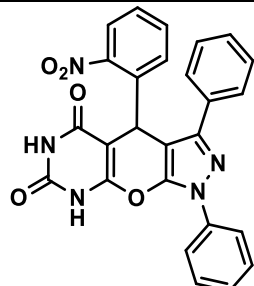
| 24 | | **4x** | 30 | 94% | 158-160 | NR |
| 25 | | **4y** | 25 | 95% | 228-230 | NR |
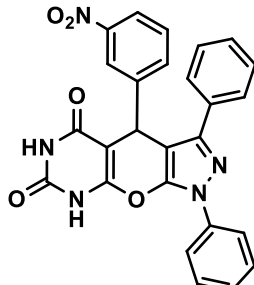
[a]Reaction conditions: barbituric acid (1 mmol), aldehyde (1 mmol), 3-substituted-5- pyrazolone (1 mmol), EtOH (5 mL) and catalyst (0.05 g) at r.t; [b]isolated yield. *NR* not reported
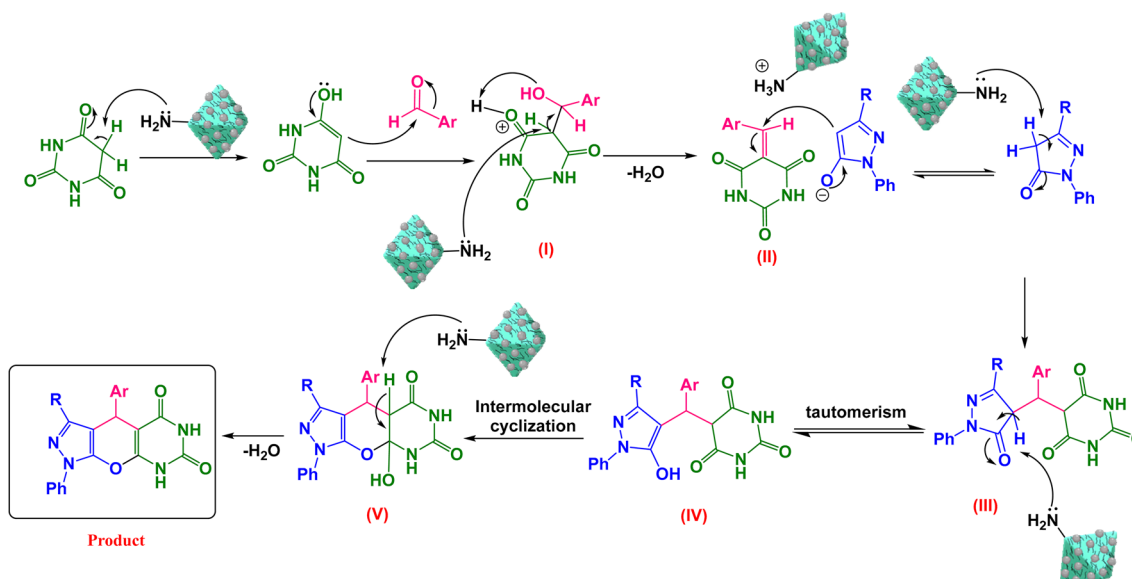
Fig. 7 The proposed mechanism for the synthesis of pyrazolopyranopyrimidines by Fe_3O_4@PmPDA@UiO-66-NH_2

3.4 Comparison with other catalysts

The catalytic efficiency of Fe_3O_4@PmPDA@UiO-66-NH_2 was evaluated in comparison with other reported catalysts for the synthesis of pyrazolopyranopyrimidines. To demonstrate the efficiency of this catalyst compared to the previously discussed methods, derivative **4a** was chosen as a representative example (Table 3). The information shows that our method provides results comparable

to those of other studies, leading in part to higher product yields and faster response times.

3.5 In-vitro anticancer effects

Using the MTT test, we evaluated the cytotoxic effects of the synthesized compounds on cancerous and normal cell lines. To this aim, The HepG2 and NIH/3T3 fibroblast cells were treated with serial concentrations (150, 75,

Fig. 8 Fe3O4@PmPDA@ UiO-66-NH2 reusability in the synthesis of 4a
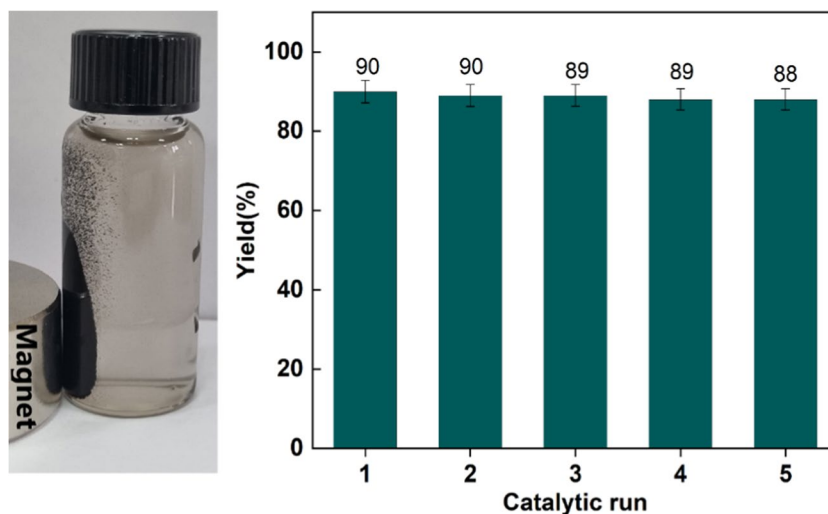
Table 3 Comparison of the catalytic efficiency of $Fe_3O_4@$ $PmPDA@UiO$-66-NH_2 with different catalysts for the synthesis of 4a

Entry	Catalyst	Condition	Yield %	Time (Min.)	Ref.
1	$Fe_3O_4@PmPDA@UiO$-66-NH_2	EtOH /r.t.	90	60	This study
2	Choline chloride: urea	EtOH /80°C	84	60	[45]
3	Silica supported phosphotungstic acid	H_2O: EtOH	96	160	[64]
4	Cellulose supported acidic ionic liquid	EtOH /80°C	90	35	[62]
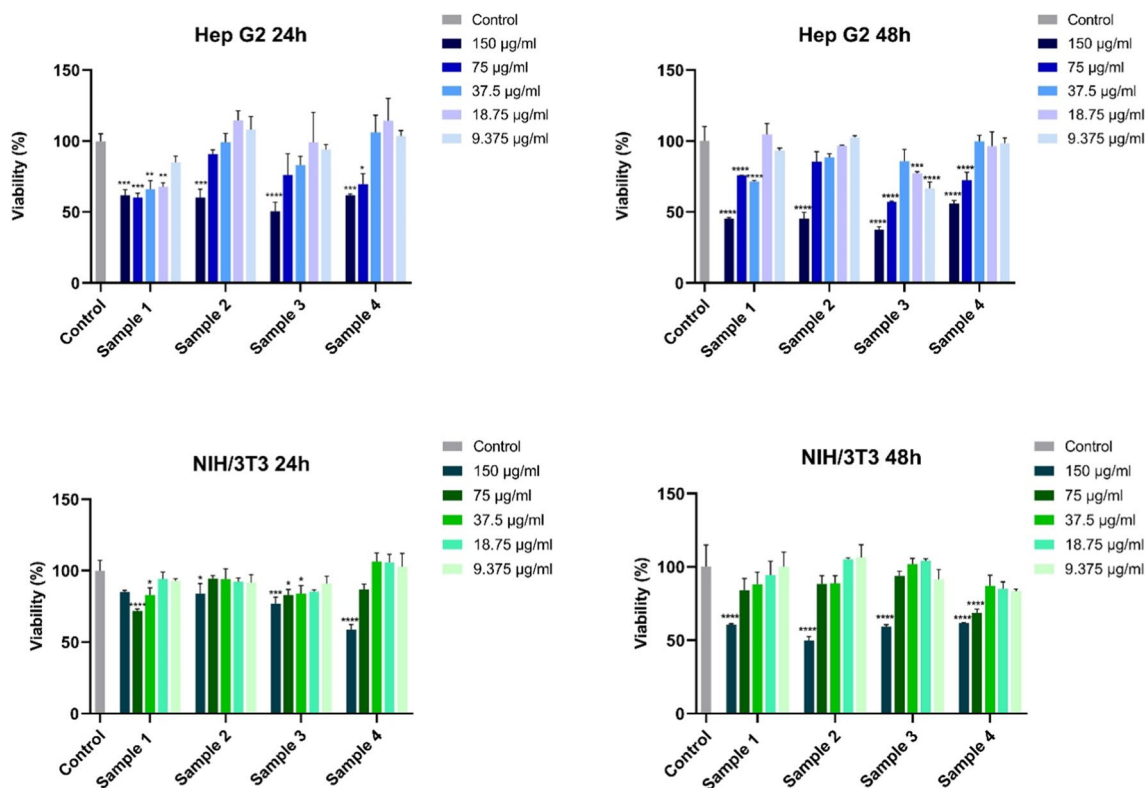
Fig. 9 Cellular toxicity assessment of samples 1-4 using MTT assay in HepG2 and fibroblast cells after 24 and 48 h of incubation. Data are represented as mean +- SD ($n = 3$). * $p < 0.05$, ** $p < 0.01$, *** $p < 0.001$ and **** $p < 0.0001$ compared with control group

Table 4 In vitro cytotoxicity effect (IC50) of samples 1–4 against HEPG2 and fibroblast cells after 24 h and 48 h of treatment

Sample	Code	Cell	Time(h)	
			24	48
1	4c	HepG2	361.7	137.5
		Fibroblast	1848	216.3
2	4g	HepG2	175.2	141.2
		Fibroblast	71,754	151.2
3	4L	HepG2	162.5	118.2
		Fibroblast	6886	167.0
4	4t	HepG2	175.4	164.9
		Fibroblast	169.1	372.4

37.5, 18.75, 9.375 µg/mL) of each sample for 24 and 48 h. Figure 9 indicates that the viability of HepG2 cells was affected dose- and time-dependent, showing a decrease in the percentage of viable cells when treated with samples 1–4 compared to untreated cells ($p < 0.001$). Based on our results, a greater inhibition of cell viability was obtained after 48 h of incubation with higher concentrations of synthesized compounds, demonstrating the anti-proliferative effects of these agents. Additionally, in most cases, the viability of fibroblast cells exhibited a comparatively minor decline when incubated with samples 1–4 as opposed to HepG2 cells. As a result, synthesized compounds hold the capability to eradicate cancerous cells while imposing minimal detrimental effects on healthy cells.

The 50% inhibition concentrations (IC50) of samples 1–4 were also calculated and reported in Table 4. Our findings demonstrate that the treatment with samples 1 and 3 accompanied the highest cytotoxic effects on HepG2 cells, while they imposed significantly lower cytotoxic effects on fibroblast cells after 24 h and 48 h. Based on estimated IC50 values, sample 2 and sample 4 cells showed less preferential antiproliferative activities

against cancer cells and provided a narrower therapeutic window for the treatments of malignant cells.

3.6 Antioxidant activity

The antioxidant properties of organic compounds can enhance their potential applications in pharmaceuticals, as well as in the food and packaging industries. Therefore, the antioxidant activity of pyrazolopyranopyrimidines was assessed using a DPPH solution (Fig. 10).

The interaction of antioxidants with DPPH results in the pairing of the stable free radical in the presence of a hydrogen donor. This reaction leads to the reduction of DPPH to hydrazine (DPPH-H). This analysis allows us to determine to what extent the pyrazolopyranopyrimidines were able to neutralize the DPPH radicals, indicating their antioxidant potential [52]. The presence of ─OH substituent on the aromatic ring and benzylic proton in the structure of the compounds also increases their antioxidant activity [67]. The results indicate that most of the derivatives exhibit antioxidant properties, with activity levels ranging from 85.3 to 98.3%.

3.7 Antibacterial activity

The antibacterial properties of the pyrazolopyranopyrimidines (**4a**, **4b**, **4c**, **4g**, **4i**, **4j**, **4L**, and **4m**) were investigated against *Staphylococcus aureus* (*S. aureus*) and *Escherichia coli* (*E. coli*). Figure 11; Table 5 display the results. Aztreonam, tetracycline, imipenem, nitrofurantoin, and rifampin were utilized as positive controls. All pyrazolopyranopyrimidine samples showed good antibacterial activity against *Staphylococcus aureus* (Gram-positive), while samples **4j** and **4b** did not affect the Gram-negative bacterium *Escherichia coli*.

Fig. 10 The photographs and the histograms of the antioxidant activity of synthesized pyrazolopyranopyrimidines
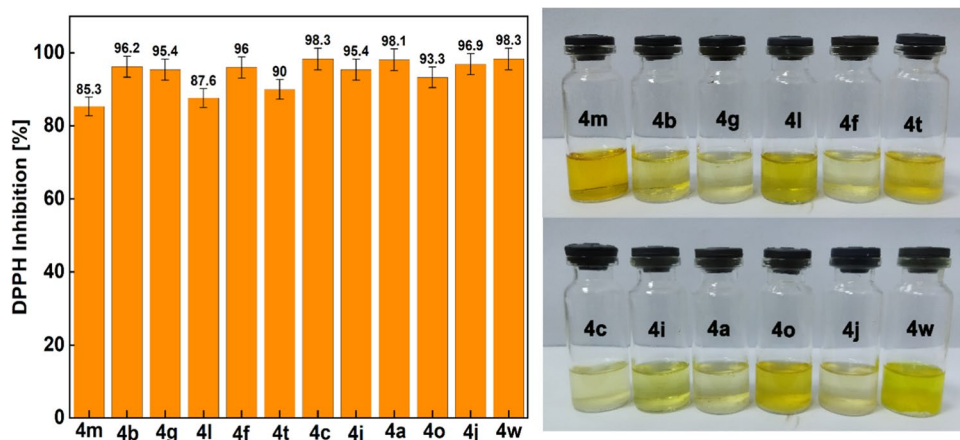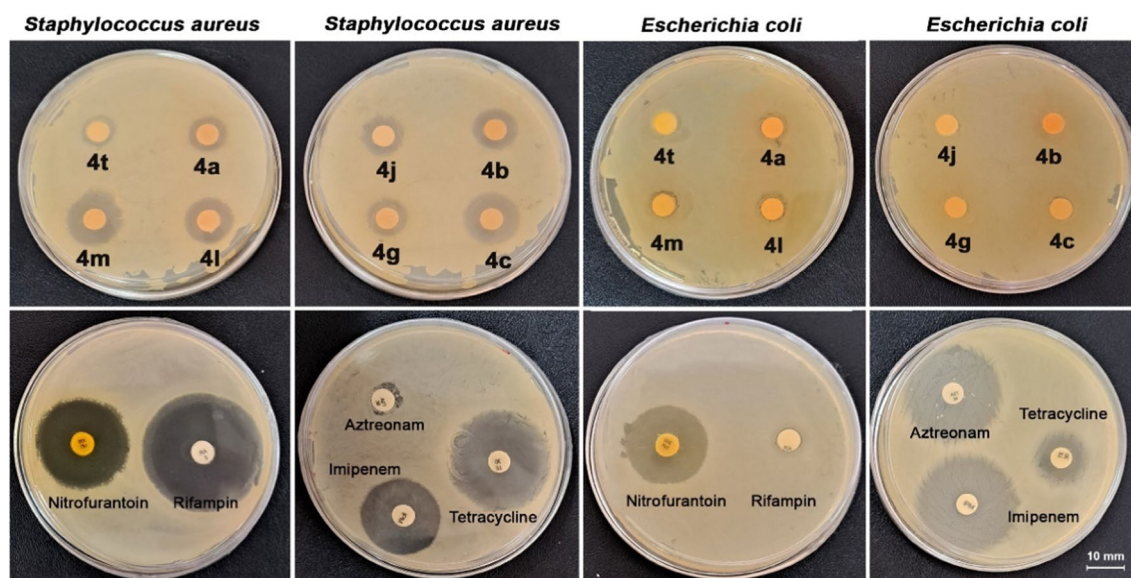
Fig. 11 Antibacterial activities of some pyrazolopyranopyrimidines against *Escherichia coli* and *Staphylococcus aureus* via Kirby–Bauer disk diffusion technique

Table 5 Antibacterial activities of some pyrazolopyranopyrimidines via Kirby–Bauer disk diffusion technique

Compound	Inhibition Zone (mm)	
	Staphylococcus aureus Gram-Positive (+)	*Escherichia coli* Gram-Negative (-)
4a	13 ± 5.0	10 ± 1.5
4b	15 ± 4.5	NE[a]
4c	18 ± 5.0	6 ± 1.5
4g	13 ± 1.2	7 ± 0.5
4j	10 ± 0.7	NE
4l	16 ± 5.0	10 ± 1.1
4m	19 ± 2.0	10 ± 0.5
4t	12 ± 4.5	10 ± 1.1
Aztreonam	9 ± 0.7	26 ± 0.1
Tetracycline	27 ± 0.9	15 ± 0.9
Imipenem	22 ± 0.4	28 ± 0.8
Nitrofurantoin	25 ± 0.8	23 ± 0.3
Rifampin	33 ± 0.4	8 ± 0.2

[a]No effect

4 Conclusion

The Fe_3O_4@P*m*PDA@UiO-66-NH_2 nanocomposite demonstrated significant catalytic activity in the one-pot, three-component condensation reaction for synthesizing pyrazolopyranopyrimidines. FESEM imaging revealed that the MOF cages were effectively coated with polymers and nanoparticles, ensuring a well-distributed catalytic surface. TGA confirmed the high thermal stability of the catalyst, crucial for maintaining catalytic activity under reaction conditions. Using 0.05 g of the catalyst, reactions were completed within 15 to 80 min, achieving product yields exceeding 90% under optimal conditions. The advantages of this reaction are simple handling and work-up procedures, high yields, and the reusability of the catalyst. The MTT assay indicated that the synthesized pyrazolopyranopyrimidines significantly reduced the survival rate of HepG2 cancer cells while exhibiting minimal cytotoxicity towards normal cells. The antioxidant capacity of the pyrazolopyranopyrimidines ranged from 85.3 to 98.3%, demonstrating their potential for mitigating oxidative stress. In addition, Pyrazolopyranopyrimidines showed notable antimicrobial effects, with inhibition zones of 19 ± 2.0 mm against *Staphylococcus aureus* and 10 ± 1.5 mm against *Escherichia coli*, highlighting their effectiveness in combating bacterial infections.

Limitations of this work include: (I) The Fe_3O_4@P*m*PDA@UiO-66-NH_2 nanocomposite was synthesized at a laboratory scale. Scaling up this process to industrial levels while maintaining catalyst effectiveness and uniformity remains a challenge. (II) Although the catalyst shows good thermal and chemical stability, further studies are needed to understand its long-term stability and performance over multiple uses. (III) Initial biological tests are promising; however, more detailed studies, including in vivo tests and an understanding of the mechanism of action, are needed to fully grasp the biological effects. Thus, further research should focus on improving the synthesis for larger-scale production and exploring the catalyst's performance in practical applications.

Additionally, understanding the mechanisms behind both the catalytic and biological activities of the synthesized compounds is crucial for optimizing their effectiveness.

Declarations

Competing interests The authors declare no competing interests.

References

1. Sethi K, Sharma S, Roy I (2016) Nanoscale iron carboxylate metal organic frameworks as drug carriers for magnetically aided intracellular delivery. RSC Adv 6:76861–76866. https://doi.org/10.1039/c6ra18480d

2. Abánades Lázaro I, Wells CJR, Forgan RS (2020) Multivariate modulation of the zr MOF UiO-66 for defect-controlled combination anticancer drug delivery. Angew Chemie 132:5249–5255. https://doi.org/10.1002/ange.201915848

3. Kazemi A, Hossein M, Hasan A (2024) Correction: tunable zn – MOF – 74 nanocarriers coated with sodium alginate as versatile drug carriers correction to : Polymer Bulletin, Polym. Bull 2–7. https://doi.org/10.1007/s00289-024-05466-9

4. Kazemi A, Afshari MH, Baesmat H, Bozorgnia B, Manteghi F, Nabipour H, Rohani S, Aliabadi HAM, Adibzadeh S, Saeb MR (2024) Polydopamine-coated Zn-MOF-74 nanocarriers: versatile drug delivery systems with enhanced biocompatibility and cancer therapeutic efficacy. J Inorg Organomet Polym Mater. https://doi.org/10.1007/s10904-024-03173-6

5. Tingting HH, Wang X, Li W, Dai Y, Fang (2015) Enhanced adsorption of Dibenzothiophene with Zinc/Copper-Based metalorganic frameworks. J Mater Chem A 6:121. https://doi.org/10.1039/C5TA05204A

6. Behrens K, Mondal SS, Nöske R, Baburin IA, Leoni S, Günter C, Weber J, Holdt HJ (2015) Microwave-assisted synthesis of defects metal-imidazolate-amide-imidate frameworks and improved CO2 capture. Inorg Chem 54:10073–10080. https://doi.org/10.1021/acs.inorgchem.5b01952

7. Sobhi HR, Yeganeh M, Ghambarian M, Fallah S, Esrafili A (2024) A new MOF-based modified adsorbent for the efficient removal of hg(ii) ions from aqueous media: isotherms and kinetics. RSC Adv 14:16617–16623. https://doi.org/10.1039/d4ra00770k

8. Lustig WP, Mukherjee S, Rudd ND, Desai AV, Li J, Ghosh SK (2017) Metal-organic frameworks: functional luminescent and photonic materials for sensing applications. Chem Soc Rev 46:3242–3285. https://doi.org/10.1039/c6cs00930a

9. Zhao SN, Song XZ, Zhu M, Meng X, Wu LL, Feng J, Song SY, Zhang HJ (2015) Encapsulation of LnIII Ions/Dyes within a Microporous Anionic MOF by Post-synthetic Ionic exchange serving as a LnIII Ion Probe and two-color luminescent sensors. Chem - A Eur J 21(27):9748–9752. https://doi.org/10.1002/chem.201500562

10. Bhuyan A, Ahmaruzzaman M (2024) Ultrasonic-assisted synthesis of highly efficient and robust metal oxide QDs immobilized-MOF-5/Ni-Co-LDH photocatalyst for sunlight-mediated degradation of multiple toxic dyes. J Alloys Compd 972:172781. https://doi.org/10.1016/j.jallcom.2023.172781

11. Sheikhsamany R, Nezamzadeh-Ejhieh A, Ensandoost R, Kakavandi B (2024) BaTi0.85Zr0.15O3/MOF-5 nanocomposite: synthesis, characterization and photocatalytic activity toward tetracycline. J Mol Liq 403:124850. https://doi.org/10.1016/j.molliq.2024.124850

12. Socha BN, Patankar B, Raj A, Palan RB, Valand J, Patel RH (2024) Krishn Jha, efficient green one-pot MOF synthesis for ultra-fast wastewater treatment and industrial catalytic bag. Chem Eng J 493:152566. https://doi.org/10.1016/j.cej.2024.152566

13. Li H, Wang K, Sun Y, Lollar CT, Li J, Zhou HC (2018) Recent advances in gas storage and separation using metal–organic frameworks. Mater Today 21:108–121. https://doi.org/10.1016/j.mattod.2017.07.006

14. Mirzaei S, LotfiKatooli L, Ahmadpour A, Niknam Shahrak M, Haghbin MR, Arami-Niya A (2024) Enhancing energy carrier gas storage: novel MOF-decorated carbons with high affinity toward methane and hydrogen. Chem Eng Res Des 203:419–430. https://doi.org/10.1016/j.cherd.2024.01.049

15. Kazemi A, Moghadaskhou F, Pordsari MA, Manteghi F, Tadjarodi A, Ghaemi A (2023) Enhanced CO2 capture potential of UiO-66-NH2 synthesized by sonochemical method: experimental findings and performance evaluation. Sci Rep 13:1–16. https://doi.org/10.1038/s41598-023-47221-6

16. Kazemi A, Ashourzadeh M, Tamtaji M, Manteghi F, Ghaemi A, Rohani S, Goddard WA (2024) Unveiling the power of defect engineering in MOF-808 to enhance efficient carbon dioxide adsorption and separation by harnessing the potential of DFT analysis. Chem Eng J 494:153049. https://doi.org/10.1016/j.cej.2024.153049

17. Bai Y, Dou Y, Xie LH, Rutledge W, Li JR, Zhou HC (2016) Zr-based metal-organic frameworks: design, synthesis, structure, and applications. Chem Soc Rev 45:2327–2367. https://doi.org/10.1039/c5cs00837a

18. De Wu C, Zhao M (2017) Incorporation of molecular catalysts in metal–organic frameworks for highly efficient Heterogeneous Catalysis. Adv Mater 29:1605446. https://doi.org/10.1002/adma.201605446

19. Mohammadi L, Vaezi MR (2023) Palladium nanoparticle-decorated Porous Metal-Organic-Framework (Zr)@Guanidine: novel efficient Catalyst in Cross-coupling (Suzuki, heck, and Sonogashira) reactions and Carbonylative Sonogashira under mild conditions. ACS Omega 8:16395–16410. https://doi.org/10.1021/acsomega.3c01179

20. Mohammadi L, Taghavi R, Hosseinifard M (2023) Stabilization of Pd NPs over the surface of b-cyclodextrin incorporated UiO-66-NH2 for the C–C coupling reaction. RSC Adv 13:17143–17154. https://doi.org/10.1039/d2ra08347g

21. Sun ZH, Chen W, Qian BB, Wang L, Yu B, Chen Q, He MY, Zhang ZH (2020) UiO-66 microcrystals catalyzed direct arylation of enol acetates and heteroarenes with aryl diazonium salts in water. Appl Organomet Chem 34:1–8. https://doi.org/10.1002/aoc.5482

22. Yarahmadi H, Salamah SK, Kheimi M (2023) Synthesis of an efficient MOF catalyst for the degradation of OPDs using TPA derived from PET waste bottles. Sci Rep 13:1–15. https://doi.org/10.1038/s41598-023-46635-6

23. Silva CG, Luz I, Llabrés FX, Xamena I, Corma A, García H (2010) Water stable Zr-Benzenedicarboxylate metal-organic frameworks as photocatalysts for hydrogen generation. Chem - Eur J 16:11133–11138. https://doi.org/10.1002/chem.200903526

24. Chen Z, Wu Q, Zhang H (2021) Novel Co/UiO-66 metal organic framework catalyst for oxygen reduction reaction in microbial fuel cells. E3S Web Conf 245:03017. https://doi.org/10.1051/e3sconf/202124503017

25. Mohammadi L, Taghavi R, Hosseinifard M, Vaezi MR, Rostamnia S (2023) Stabilization of pd NPs over the surface of β-cyclodextrin incorporated UiO-66-NH2 for the C-C coupling reaction. RSC Adv 13:17143–17154. https://doi.org/10.1039/d2ra08347g

26. Hajek J, Vandichel M, Van De Voorde B, Bueken B, De Vos D, Waroquier M, Van Speybroeck V (2015) Mechanistic studies of aldol condensations in UiO-66 and UiO-66-NH2 metal organic frameworks. J Catal 331:1–12. https://doi.org/10.1016/j.jcat.2015.08.015

27. Ali-Ahmad A, Hamieh T, Roques-Carmes T, Hmadeh M, Toufaily J (2023) Effect of modulation and functionalization of UiO-66 Type MOFs on their surface Thermodynamic properties and Lewis Acid–Base behavior. Catalysts 13:205. https://doi.org/10.3390/catal13010205

28. Wiśniewska P, Haponiuk J, Saeb MR, Rabiee N, Bencherif SA (2023) Mitigating metal-organic framework (MOF) toxicity for biomedical applications. Chem Eng J 471:144400. https://doi.org/10.1016/j.cej.2023.144400

29. Al-Omoush MK, Polozhentsev OE, Soldatov AV (2024) Fabrication of cisplatin-loaded core–shell Fe3O4@UiO-66-NH2 magnetic nanocomposite for potential drug delivery. Polyhedron 256:116999. https://doi.org/10.1016/j.poly.2024.116999

30. Hong J, Wang L, Zheng Q, Cai C, Yang X, Liao Z (2024) The recent applications of magnetic nanoparticles in biomedical fields. Mater (Basel) 17:2870. https://doi.org/10.3390/ma17122870

31. Behrens S, Appel I (2016) Magnetic nanocomposites. Curr Opin Biotechnol 39:89–96. https://doi.org/10.1016/j.copbio.2016.02.005

32. Zhu Y, Stubbs LP, Ho F, Liu R, Ship CP, Maguire JA, Hosmane NS (2010) Magnetic nanocomposites: a new perspective in catalysis. ChemCatChem 2:365–374. https://doi.org/10.1002/cctc.200900314

33. Shukla R, Sharma P, Fageria A, Chowdhury L (2019) Novel Spiro/non-Spiro Pyranopyrazoles: eco-friendly synthesis, In-vitro anticancer activity, DNA binding, and In-silico docking studies no title. Curr Bioact Compd 15:257–267. https://doi.org/10.2174/1573407213666170828165512

34. Das D, Banerjee R, Mitra A (2014) Bioactive and pharmacologically important pyrano [2, 3-c] pyrazoles. J Chem Pharm Res 6(11):108–116

35. Reddy GM, Sravya G, Yuvaraja G, Camilo A, Zyryanov GV, Garcia JR (2018) Highly functionalized pyranopyrazoles: synthesis, antimicrobial activity, simulation studies and their structure activity relationships (SARs). Res Chem Intermed 44:7491–7507. https://doi.org/10.1007/s11164-018-3569-8

36. Capodanno D, Ferreiro JL, Angiolillo DJ (2013) Antiplatelet therapy: new pharmacological agents and changing paradigms. J Thromb Haemost 11:316–329. https://doi.org/10.1111/jth.12219

37. Aliabadi RS, Mahmoodi NO (2016) Green and efficient synthesis of pyranopyrazoles using [bmim][OH-] as an ionic liquid catalyst in water under microwave irradiation and investigation of their antioxidant activity. RSC Adv 6:85877–85884. https://doi.org/10.1039/c6ra17594e

38. Hernández-Vázquez E, Ocampo-Montalban H, Cerón-Romero L, Cruz M, Gómez-Zamudio J, Hiriart-Valencia G, Villalobos-Molina R, Flores-Flores A, Estrada-Soto S (2017) Antidiabetic, antidyslipidemic and toxicity profile of ENV-2: a potent pyrazole derivative against diabetes and related diseases. Eur J Pharmacol 803:159–166. https://doi.org/10.1016/j.ejphar.2017.03.036

39. Fayed EA, Nosseir ES, Atef A (2022) El–Kalyoubi, in vitro anti-microbial evaluation and in silico studies of coumarin derivatives tagged with pyrano-pyridine and pyrano-pyrimidine moieties as DNA gyrase inhibitors. Mol Divers 26:341–363. https://doi.org/10.1007/s11030-021-10224-4

40. Abd El-Sattar NEA, El-Adl K, El-Hashash MA, Salama SA, Elhady MM (2021) Design, synthesis, molecular docking and in silico ADMET profile of pyrano[2,3-d]pyrimidine derivatives as antimicrobial and anticancer agents. Bioorg Chem 115:105186. https://doi.org/10.1016/j.bioorg.2021.105186

41. Bhat AR, Shalla AH, Dongre RS (2015) Microwave assisted one-pot catalyst free green synthesis of new methyl-7-amino-4-oxo-5-phenyl-2-thioxo-2,3,4,5-tetrahydro-1H-pyrano[2,3-d]pyrimidine-6-carboxylates as potent in vitro antibacterial and anti-fungal activity. J Adv Res 6:941–948. https://doi.org/10.1016/j.jare.2014.10.007

42. Patil P, Yadav A, Bavkar L, N NB, Satyanarayan ND, Mane A, Gurav A, Hangirgekar S, Sankpal S (2021) [MerDABCO-SO3H] cl catalyzed synthesis, antimicrobial and antioxidant evaluation and molecular docking study of pyrazolopyranopyrimidines. J Mol Struct 1242:130672. https://doi.org/10.1016/j.molstruc.2021.130672

43. Rigi F, Shaterian HR (2022) A novel triazole bonded silica heterogeneous catalyst for the one-pot synthesis of Pyrazolopyranopyrimidines and Dihydro-1 H-pyrano [2, 3-c] pyrazol-6-ones. Chem Afr 5:1255–1263. https://doi.org/10.1007/s42250-022-00408-2

44. Mir F, Hazeri N, Maghsoodlou MT, Lashkari M (2022) Synthesis of Pyrazolopyranopyrimidine and Dihydropyrano[2,3-c]pyrazole derivatives using Fe3O4@THAM-Piperazine as a superparamagnetic nanocatalyst under green condition. Polycycl Aromat Compd 43:5375–5390. https://doi.org/10.1080/10406638.2022.2101488

45. Tipale MR, Khillare LD, Deshmukh AR, Bhosle MR (2018) An efficient four component domino synthesis of Pyrazolopyranopyrimidines using recyclable choline chloride: urea deep eutectic solvent. J Heterocycl Chem 55:716–728. https://doi.org/10.1002/jhet.3095

46. Akolkar SV, Kharat ND, Nagargoje AA, Subhedar DD, Shingate BB (2020) Ultrasound-assisted β-Cyclodextrin Catalyzed One-Pot Cascade synthesis of Pyrazolopyranopyrimidines in water. Catal Lett 150:450–460. https://doi.org/10.1007/s10562-019-02968-4

47. Keshavarz M, Mamaghani M, Dekamin MG, Nikpassand M (2021) Tetramethylguanidine-functionalized nanosize γ-Al2O3 as a novel and efficient catalyst for the four-component synthesis of pyrazolopyranopyrimidine derivatives. J Iran Chem Soc 18:1419–1431. https://doi.org/10.1007/s13738-020-02123-6

48. Rostami H, Shiri L (2019) CoFe2O4@ SiO2-PA-CC-Guanidine MNPs as an efficient catalyst for the one-pot four-component synthesis of Pyrazolopyranopyrimidines. ChemSel 4:8410–8415. https://doi.org/10.1002/slct.201901925

49. Honari M, Sanaeishoar H, Kiasat AR, Mohammadi MK (2021) Efficient synthesis of pyrazolopyranopyrimidines using DBU-based nanomagnetic catalyst. Res Chem Intermed 47:1829–1841. https://doi.org/10.1007/s11164-021-04397-8

50. Amini H, Neamani S, Moradi L (2021) Green synthesis of Pyrazolo Pyrano Pyrimidine derivatives using ZnFe2O4/GA as a new effective catalyst in water media. ChemSel 6:9608–9615. https://doi.org/10.1002/slct.202101980

51. Nazarzadeh Zare E, Mansour Lakouraj M, Mohseni M (2014) Biodegradable polypyrrole/dextrin conductive nanocomposite: synthesis, characterization, antioxidant and antibacterial activity. Synth Met 187:9–16. https://doi.org/10.1016/j.synthmet.2013.09.045

52. Das D, Nath BC, Phukon P, Dolui SK (2013) Synthesis and evaluation of antioxidant and antibacterial behavior of CuO

nanoparticles. Colloids Surf B Biointerfaces 101:430–433. https://doi.org/10.1016/j.colsurfb.2012.07.002

53. Seidi F, Arabi Shamsabadi A, Dadashi Firouzjaei M, Elliott M, Saeb MR, Huang Y, Li C, Xiao H, Anasori B (2023) MXenes antibacterial properties and applications: a review and perspective. Small 19:1–32. https://doi.org/10.1002/smll.202206716

54. Boroujerdian M, Rahimi S, Mirani Nezhad S, Pourmousavi SA, Nazarzadeh Zare E, Salimi F, Amirahmadi F, Daneshgar H (2023) CoFe2O4@SiO2–NH2@MOF-5 magnetic nanocatalyst for the synthesis of biologically active quinazoline derivatives. Environ Res 236:116708. https://doi.org/10.1016/j.envres.2023.116708

55. Aghajanzadeh M, Zamani M, Molavi H, Khieri Manjili H, Danafar H, Shojaei A (2018) Preparation of metal–organic frameworks UiO-66 for adsorptive removal of Methotrexate from Aqueous solution. J Inorg Organomet Polym Mater 28:177–186. https://doi.org/10.1007/s10904-017-0709-3

56. Shanahan J, Kissel DS, Sullivan E (2020) PANI@UiO-66 and PANI@UiO-66-NH2Polymer-MOF hybrid composites as tunable semiconducting materials. ACS Omega 5:6395–6404. https://doi.org/10.1021/acsomega.9b03834

57. Nezhad SM, Pourmousavi SA, Zare EN (2021) Superparamagnetic poly(aniline-co-m-phenylenediamine)@Fe3O4 nanocomposite as an efficient Heterogeneous Catalyst for the synthesis of 1H-pyrazolo[1,2-a]pyridazine-5,8-diones & 1H-pyrazolo[1,2-b]phthalazine-5, 10-diones derivatives. Curr Org Synth 19:246–266. https://doi.org/10.2174/1570179418666211104143736

58. Liu M, Ye Y, Ye J, Gao T, Wang D, Chen G, Song Z (2023) Recent advances of Magnetite (Fe3O4)-Based magnetic materials in catalytic applications. Magnetochemistry 9:110. https://doi.org/10.3390/magnetochemistry9040110

59. Rabiee N, Bagherzadeh M, Heidarian Haris M, Ghadiri AM, Matloubi Moghaddam F, Fatahi Y, Dinarvand R, Jarahiyan A, Ahmadi S, Shokouhimehr M (2021) Polymer-coated NH2-UiO-66 for the codelivery of DOX/pCRISPR. ACS Appl Mater Interfaces 13:10796–10811. https://doi.org/10.1021/acsami.1c01460

60. Sekopelo AG, Munonde TS, Nqombolo A, Mpupa A, Nomngongo PN (2024) UiO-66@Fe3O4 nanocomposite as an adsorbent in dispersive solid phase extraction of metformin in surface water and wastewater. Nano Express 5:025011. https://doi.org/10.1088/2632-959X/ad461c

61. Amador C, Martin de L, Juan (2016) Strategies for structured Particulate Systems Design. Elsevier. https://doi.org/10.1016/B978-0-444-63683-6.00019-8

62. Francis P, Rivnay J, Salleo A, Stingelin N, Silva C (2015) Multiphase semicrystalline microstructures drive exciton dissociation in neat plastic semiconductors. J Mater Chem C 3:10715–10722. https://doi.org/10.1039/b000000x

63. Heravi MM, Daraie M (2016) A novel and efficient five-component synthesis of pyrazole based pyrido[2,3-d]pyrimidine-diones in water: a triply green synthesis. Molecules 21:441. https://doi.org/10.3390/molecules21040441

64. Swami MB, Karad AR, Ganapure SD, Jadhav AH, Patil SG (2023) Silica supported phosphotungstic acid catalyzed one pot efficient synthesis of pyrazolopyranopyrimidine derivatives. Mater Today Proc 73:508–514. https://doi.org/10.1016/j.matpr.2022.11.375

65. Ghorbani-Choghamarani A, Kakakhani Z, Taherinia Z (2023) 4,6-Diamino-2-thiopyrimidine-based Cobalt Metal Organic Framework (Co-DAT-MOF): green, efficient, novel and reusable nanocatalyst for synthesis of multicomponent reactions. Sci Rep 13:7502. https://doi.org/10.1038/s41598-023-34001-5

66. Moradi L, Mahdipour P (2019) Green and rapid synthesis of dihydropyrimido [4,5-b]quinolinetrione derivatives using CoFe2O4@PPA as high efficient solid acidic catalyst under ultrasonic irradiation. Appl Organomet Chem 33:1–14. https://doi.org/10.1002/aoc.4996

67. Bērziņa L, Mieriņa I (2023) Antiradical and antioxidant activity of compounds containing 1,3-Dicarbonyl Moiety: an overview Molecules 28:1–29. https://doi.org/10.3390/molecules28176203

Spectroscopic Data

All Spectroscopic Data can be seen in the supporting information.

Authors and Affiliations

Yi Xu[1] · Shefa Mirani Nezhad[2] · Ehsan Nazarzadeh Zare[2] · Seied Ali Pourmousavi[2] · Alireza Doostian[3] · Junna Ren[4] · Ana Cláudia Paiva-Santos[5,6] · Aimin Wu[7] · Gautam Sethi[8] · Filippo Rossi[9] · Xiangdong Wang[10] · Pooyan Makvandi[11]

✉ Ehsan Nazarzadeh Zare
ehsan.nazarzadehzare@gmail.com; e.nazarzadeh@du.ac.ir

✉ Pooyan Makvandi
Pooyan.makvandi@wmu.edu.cn

[1] Department of Urology, NanoBiomedical Group, The Quzhou Affiliated Hospital of Wenzhou Medical University, Quzhou People's Hospital, Quzhou, China

[2] School of Chemistry, Damghan University, Damghan 36716-45667, Iran

[3] Iran University of Medical Sciences, Tehran, Iran

[4] College of Materials Science and Engineering, Taiyuan University of Science and Technology, Taiyuan 030024, China

[5] Department of Pharmaceutical Technology, Faculty of Pharmacy of the University of Coimbra, University of Coimbra, Coimbra 3000-548, Portugal

[6] REQUIMTE/LAQV, Group of Pharmaceutical Technology, Faculty of Pharmacy of the University of Coimbra, University of Coimbra, Coimbra, Portugal

[7] Department of Orthopaedics, Key Laboratory of Orthopaedics of Zhejiang Province, The Second Affiliated Hospital, Yuying Children's Hospital of Wenzhou Medical University, Wenzhou 325000, Zhejiang, China

[8] Department of Pharmacology and NUS Centre for Cancer Research (N2CR), Yong Loo Lin School of Medicine, National University of Singapore, Singapore 117600, Singapore

[9] Department of Chemistry, Materials and Chemical Engineering, Politecnico di Milano Technical University, Milano 20133, Italy

[10] Department of Pulmonary and Critical Care Medicine, Zhongshan Hospital, Fudan University Shanghai Medical College, Shanghai 200032, China

[11] The Quzhou Affiliated Hospital of Wenzhou Medical University, Quzhou People's Hospital, Quzhou 324000, Zhejiang, China